

Special Collection

Tris(trimethylsilyl) Phosphite and Lithium Difluoro(oxalato)borate as Electrolyte Additives for LiNi_{0.5}Mn_{1.5}O₄-Graphite Lithium-Ion Batteries

Ali Jamal,^[a] Girish D. Salian,^[a] Alma Mathew,^[a] Wandu Wahyudi,^[a] Rodrigo P. Carvalho,^[a] Ritambhara Gond,^[a] Satu Kristiina Heiskanen,^[b] Daniel Brandell,^[a] and Reza Younesi^{*[a]}

Raising the energy density of lithium-ion batteries (LIBs) through the operation of high-voltage cathodes presents a challenge in terms of practical use due to electrolyte degradation. Consequently, it is imperative to explore new materials to circumvent this issue. In this study, a combination of tris(trimethylsilyl) phosphite (TMSPi) and lithium difluoro(oxalato)borate (LiDFOB) is presented as film-forming additives in a conventional LiPF₆-containing carbonate-based electrolyte solution in high-voltage LiNi_{0.5}Mn_{1.5}O₄-graphite full cells. At high voltage, TMSPi oxidizes on the LiNi_{0.5}Mn_{1.5}O₄ (LNMO) cathode surface prior to the decomposition of electrolyte solvents, promoting the formation of a stable cathode

electrolyte interphase (CEI) layer. In tandem, given that LiDFOB has a lower reduction potential than ethylene carbonate (EC), it has the possibility of forming a solid electrolyte interphase (SEI) on the graphite anode surface. Combining the two additives was found to suppress the degradation of the electrolyte to a large extent. Among the investigated concentration of the additives, the combination of 1 wt.% TMSPi and 2 wt.% LiDFOB added to LP40 electrolyte exhibits improved capacity retention of 80% after 400 cycles at 0.3 C, compared to the electrolyte with no additive with 67% capacity retention over the same period. Thereby, the combination of TMSPi with LiDFOB provides an improvement for high voltage LIBs.

Introduction

Although lithium-ion batteries (LIBs) have been used as power batteries for decades, there is desire to raise their power and energy density, especially for the electric vehicle (EV) market.^[1,2] LiNi_{0.5}Mn_{1.5}O₄ (LNMO) has been proposed as a viable cathode material due to its high-voltage (4.7 V vs. Li/Li⁺) and power density properties originating from the 3D lithium-ion diffusion channels inherent in the spinel structure of LNMO.^[3–5] However, the high electrochemical potential of LNMO is accompanied by an electrolyte parasitic reaction, as carbonate-based electrolytes have been shown to decompose severely at voltages above 4 V vs. Li/Li⁺. Decomposition products from carbonate-based electrolytes tend to accumulate on the surface of the electrode, which results in excessive battery impedance.^[6–8] In addition, lithium hexafluorophosphate (LiPF₆) reacts with the residual

amounts of water in the electrolyte and produces hydrofluoric acid (HF), which accelerates dissolution of the transition metals (Mn²⁺, Ni²⁺) in LNMO.^[9] These side reactions simultaneously cause poor cycling performance of the LNMO electrode and damage the solid electrolyte interphase (SEI) and cathode electrolyte interphase (CEI) layers.^[10,11] The use of specific electrolyte additives has proven effective in preventing the oxidation of traditional electrolyte formulas at high voltages. This is achieved through the formation of a CEI layer,^[12,13] stabilizing the electrolyte salt,^[14] scavenging corrosive impurities such as HF,^[15] or removing O₂ gas produced during high potential reactions.^[16,17]

Among the various high-voltage additives available, tris(trimethylsilyl) phosphite (TMSPi) has been introduced as an efficient bifunctional additive that could scavenge the HF generated during cycling and build a robust CEI upon its oxidative decomposition.^[18,19] Song et al. found that TMSPi prevented the dissolution of Mn²⁺ and Ni²⁺ from LiNi_{0.5}Mn_{1.5}O₄ electrodes by scavenging HF molecules at a high charge potential of 5 V.^[20] The stability of additives and their ability to build suitable electrolyte interphase layers are generally determined through oxidation and reduction potential values.^[21,22] The oxidation potential (OP) and reduction potential (RP) of TMSPi were previously calculated using density functional theory (DFT) by Yim et al.^[23] and the OP was reported as 4.29 V vs. Li/Li⁺, which is lower than that of ethylene carbonate (EC, 6.92 V vs. Li/Li⁺). Meanwhile, the RP of TMSPi is much lower than that of EC. As a result, in an electrolyte solution containing both EC and TMSPi, TMSPi should contribute to formation of CEI on the cathode, whereas EC will have the main contribute to SEI formation. In addition, due to the formation of a robust

[a] A. Jamal, Dr. G. D. Salian, A. Mathew, Dr. W. Wahyudi, Dr. R. P. Carvalho, Dr. R. Gond, Prof. D. Brandell, Assoc. Prof. R. Younesi
Department of Chemistry-Ångström Laboratory
Uppsala University
Box 538, SE-75121, Uppsala (Sweden)
E-mail: reza.younesi@kemi.uu.se

[b] Dr. S. K. Heiskanen
Volkswagen AG
38436 Wolfsburg (Germany)

Supporting information for this article is available on the WWW under <https://doi.org/10.1002/celec.202300139>

Part of a Special Collection celebrating the 140th anniversary of the Swedish Chemical Society.

© 2023 The Authors. ChemElectroChem published by Wiley-VCH GmbH. This is an open access article under the terms of the Creative Commons Attribution License, which permits use, distribution and reproduction in any medium, provided the original work is properly cited.

Si–F bond, the trimethylsilyl (TMS) group exhibits a high binding affinity towards HF, therefore it is considered as an HF scavenger.^[24]

Furthermore, lithium difluoro(oxalato)borate (LiDFOB) has also been proposed as an SEI-forming electrolyte additive and can effectively enhance the electrochemical and high-temperature performance of graphite-based negative electrodes.^[25,26] Prior studies have shown that adding LiDFOB to electrolytes can promote building a stable SEI layer on graphite anodes upon its reductive decomposition.^[27] For example, galvanostatic voltage profiles for cells with LiDFOB demonstrate a voltage plateau of about 1.7 V vs. Li/Li⁺ during the first graphite-lithiation cycle attributed to the reductive decomposition of LiDFOB.^[28] Along with forming a better SEI on the negative electrode, Fu et al. claimed that the ODFB anion in LiDFOB in LiMn₂O₄-Li cells interacts with Mn²⁺ and produces an insoluble film on the cathode surface, thus improving cell cyclability by preventing further Mn²⁺ dissolution.^[29] More recently, studies suggest that using dual additives in combination is more effective than using a single additive, since using a single additive for high voltage materials cannot provide protection simultaneously and comprehensively on both anode and cathode electrodes.^[30,31] The appropriate amount of a particular additive, however, probably depends on how it functions in the cell and how much is required to achieve the intended result without significantly impairing other cell performance-affecting characteristics.

The influence of combination of TMSPI and LiDFOB as dual additives to LP40 (1 M LiPF₆ in EC/DEC 1:1 w/w) electrolyte for LNMO-graphite full-cell is here investigated using galvanostatic cycling and nuclear magnetic resonance (NMR) spectroscopy. In addition, theoretical calculations were carried out to get a clearer insight into the mechanisms of how additives influence the battery chemistry under high voltage conditions. The CEI and SEI layers on the cathode and anode respectively were investigated using X-ray photoelectron spectroscopy (XPS). The resistance increase during cycling of the cells was determined using intermittent current interruption technique (ICI). As a result of the synergistic effects of the two additives, the high-voltage battery demonstrates improved electrochemical performance. Thereby, this research study could pave the way for

future advancements in the improvement of high-energy density LIBs.

Results and Discussion

1 wt. % TMSPI was added to the baseline electrolyte composed of 1 M LiPF₆ in 1:1 w/w ethylene carbonate (EC): diethyl carbonate (DEC) while the concentration of LiDFOB varied between 1 to 3 wt. %. Figure 1 shows the average discharge capacities versus cycle number and the respective coulombic efficiency (CE) of the full-cells with the investigated electrolytes. The cycling protocol includes three formation cycles at 0.1 C rate followed by 100 cycles at 0.3 C rate within the cycling window of 3.5 V to 4.8 V. The results show that the initial discharge capacities of all the cells containing additives are lower than the initial capacity of the baseline cell. Among all the tested combinations, the cell with 1 % TMSPI + 2 % LiDFOB appeared to achieve the best capacity retention. The cell with 1 % TMSPI + 2 % LiDFOB also provides a higher average coulombic efficiency over 100 cycles than that of the baseline cells, followed by the cell with 1 % TMSPI + 1 % LiDFOB, and then the cell with 1 % TMSPI + 3 % LiDFOB. This suggests that an excess amount of LiDFOB may lead to undesired side reactions.

Figure 2 displays the galvanostatic charge/discharge profiles of the first three formation cycles at 0.1 C rate. The CE of these cycles are provided as an inset to these graphs. Additionally, the figure shows a few selected cycles (4th, 53rd, 103rd) at 0.3 C rate. The slightly lower capacity for the cell with additives is likely due to reduction/oxidation occurring on both electrodes during interphase layer formation. This process could consume cyclable Li ions and lead to a lower CE observed in the 1st cycles for the cells with additives (see Figure 2a). The cell with 1 % TMSPI + 3 % LiDFOB showed the lowest CE of the 1st cycle (about 78 %). For all the cells, the CE increases with subsequent cycles and remains stable afterward. However, all the cells with additives showed relatively higher overpotential compared to the baseline cell in the first cycle, likely due to the formation of a more resistive interphase by the additives. After many cycles, however, all the cells show similar overpotential, though the

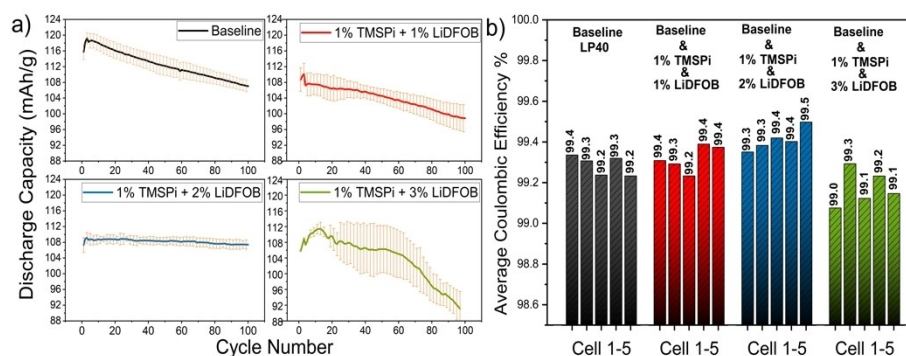


Figure 1. (a) The average discharge capacity of different concentrations of additives and the baseline electrolyte is depicted along with an error bar (vertical line) representing a standard deviation of five cells. (b) Average CE of 100 cycles of different concentrations of additives and the baseline electrolyte.

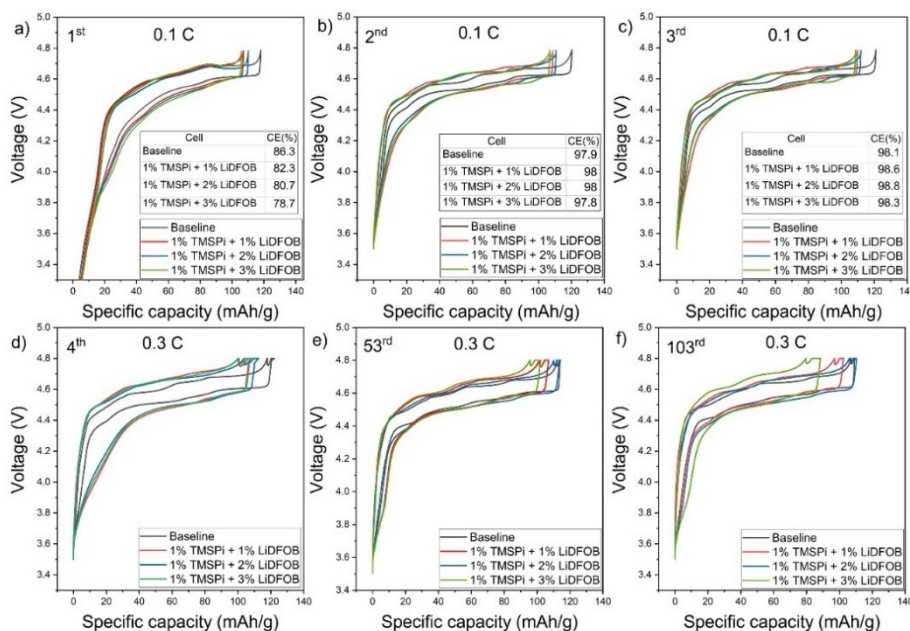


Figure 2. Galvanostatic voltage profile of the baseline cell and cells with different concentrations of additives at 0.1 C rate for the first three cycles a), b), c) and at 0.3 C rate for different cycles d), e) and f).

cell with 1% TMSPi + 3% LiDFOB showed higher overpotential after 100 cycles. This is in line with the capacity retention results in Figure 1a suggesting that an excess amount of LiDFOB may result in too high resistance and thus rapid capacity fading.

The effects of the additives on the electrolyte microstructure were studied for different percentages by NMR spectroscopy. NMR studies were conducted using a sealed D_2O insert as a lock solvent to preserve the pristine nature of the electrolyte (see Figure 3a).^[32] The chemical structures discussed in this analysis are presented in Figure 3b. Moreover, the reactivity of the additives with EC-DEC solvents was also investigated in the absence of $LiPF_6$ salt (Figure 3c–e) to isolate the effect. In general, the 1H , ^{19}F , and ^{31}P NMR spectra of the main electrolyte components EC, DEC, and $[PF_6]^-$ do not show significant change in their chemical shifts in the presence of additives (Figure S1), which could be due to their high concentration that leads to negligible change in their environment. However, the 1H NMR spectra (Figure 3c) show the trivial shielded TMSPi molecules due to interactions with the solvents, but there is no reaction observed between the additives and EC-DEC solvents, which is also corroborated by the ^{19}F and ^{31}P NMR spectra (Figures 3d and 3e). The ^{31}P NMR spectra confirm the TMSPi peak at 115.1 ppm, in addition to the presence of tris(trimethylsilyl) phosphate (TMSPa) and bis-(trimethylsilyl) phosphate (BMSPa) as possible side products both in the pristine sample and in the EC-DEC solvents at around -24.06 and -13.02 ppm, respectively.^[33] Further, the ^{19}F NMR spectra show a LiDFOB peak in the EC-DEC at around -154.9 to -155.0 ppm. Thereby, the NMR experiments indicate that there is no reaction between TMSPi and LiDFOB with the EC-DEC solvent mixture.

Moreover, we investigated the reactivity of the additives in the presence of $LiPF_6$, i.e., by adding the additives into the

baseline electrolyte (Figure 3f–h). Note that the peaks of TMSPi, TMSPa, and BMSPa from the solution without $LiPF_6$ (dashed curve in Figure 3f) shift up field towards smaller chemical shift values due to the presence of $LiPF_6$ (blue curve in Figure 3f), indicating a change in the environment of the additives after adding the $LiPF_6$ salt.^[34] TMSPi may react with $[PF_6]^-$ anions and form trimethylsilyl fluoride (TMSF), where the typical 1H and ^{19}F peaks of TMSF are observed at around 0.255 – 0.275 ppm (Figure 3f) and -158.01 ppm (Figure 3g), respectively.^[17] In contrast, LiDFOB appears to be relatively more stable in the electrolyte compared to TMSPi, as indicated by its ^{19}F NMR peaks at around -155.5 to -155.6 ppm. However, upon increasing the LiDFOB concentration, the 1H NMR peak of TMSPi at 0.238 ppm diminishes and then disappears (red dashed-line in Figure 3f), which is in-line with the corresponding TMSPi peak at 115.23 ppm in the ^{31}P NMR spectra (Figure 3g). The results suggest an interplay between $[PF_6]^-$, TMSPi, and LiDFOB in the electrolytes, which could be the reason for the improved cell performances. In particular, the interplay results in the transformation from TMSPi to TMSF, TMSPa, BMSPa, and mono(trimethylsilyl)phosphate (MMSPa). BMSPa and MMSPa are the degradation products of TMSPa with loss of one and two methyl-silyl groups from the initial TMSPa structure, respectively.^[33] Based on the ^{31}P NMR spectra (Figure 3h), formation of MMSPa and TMSPa are more favorable than BMSPa in the LP40 + 1% TMSPi + 2% LiDFOB electrolyte, which could be the reason for the most optimized stability of the long-term cell performance compared to the other electrolyte compositions. In particular, TMSPa is beneficial for HF scavenge upon cycling the batteries,^[35] while the MMSPa degradation product forms beneficial CEI components that can stabilize the electrode,^[36] as discussed in the XPS analysis section.

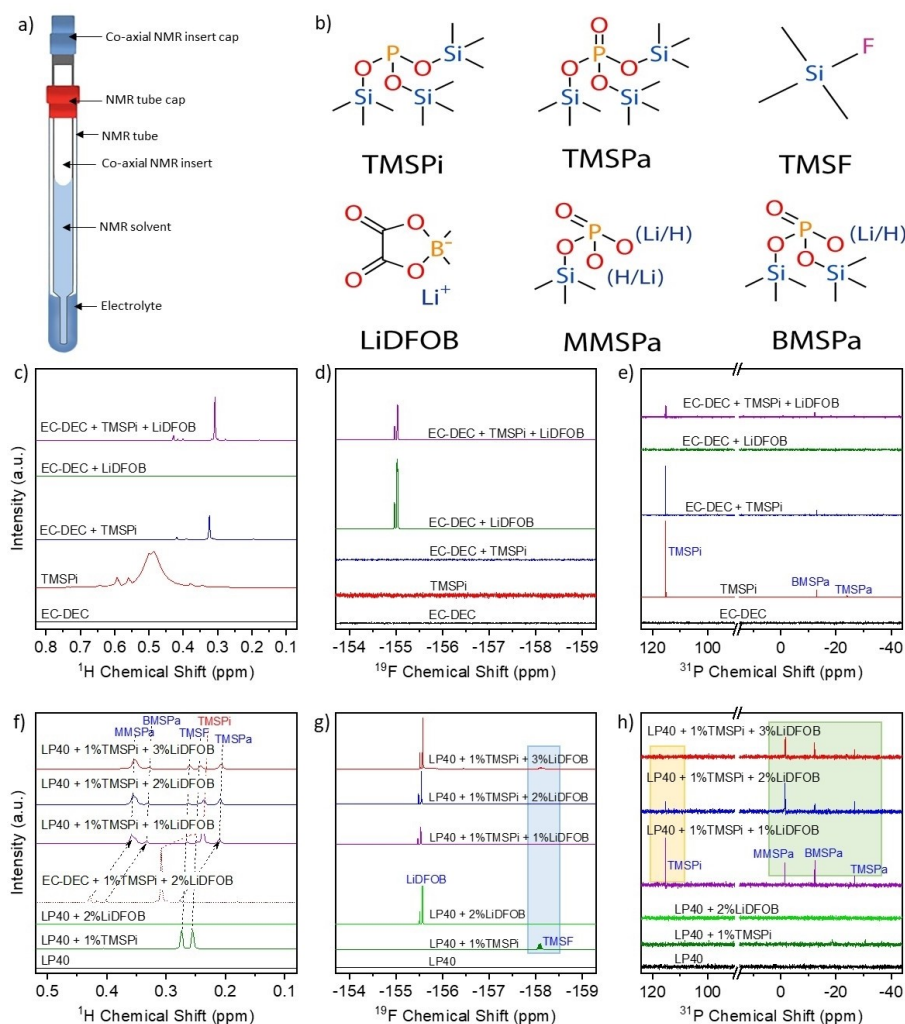


Figure 3. (a) Schematic of the NMR experimental setup. (b) Molecular structures of TMSPi, TMSPa, TMSF, LiDFOB, MMSPa, and BMSPa. (c) ^1H , (d) ^{19}F , and (e) ^{31}P NMR spectra of additives in the EC-DEC (no LiPF_6 salt). (f) ^1H , (g) ^{19}F , and (h) ^{31}P NMR spectra of additives in the baseline electrolyte.

Figure 4a shows the estimated electrochemical stability window (ESW) by DFT calculations for the following compounds, from left to right: TMSPi, LiDFOB, the electrolyte LiPF_6 :(EC/DEC), and a system composed of TMSPi:LiDFOB with the ratios 1:1, 1:2 and 1:3. A detailed description of the calculation steps is given in the Experimental Section. The zero dashed line in the plot represents the standard hydrogen electrode (SHE) reference. Graphite and LNMO electrode potentials are also displayed in the plot by different dashed lines. The 2 LiPF_6 to 1 EC/1DEC ratio was chosen to better reflect the actual salt: electrolyte composition. Comparing the TMSPi and LiDFOB separately, it is clear that the former has a lower oxidation potential as compared to the electrolyte and the LNMO cathode, while the latter has a reduction potential similar to the graphite anode and higher than the electrolyte one. This would indicate that primarily TMSPi is indeed prone to be oxidized on the interface with the LNMO cathode, while LiDFOB is prone to be reduced on the surface of graphite. Both cases appear more energetically favorable than the equivalent reactions happening with the main electrolyte components.

Therefore, these compounds would function as sacrificial products at the electrode interfaces, protecting the electrolyte from further electrochemical decomposition.

Furthermore, when a mixture of both additives is considered, these effects are further enhanced. The resulting reduction potential of the TMSPi:LiDFOB complex is higher than that of the sole LiDFOB or that of the graphite anode, which would render a reduction reaction even more favorable to occur considering the additives versus the LiPF_6 :(EC/DEC) electrolyte. On the cathode side, on the other hand, the lowest stability of the additive complex is obtained when the ratio 1:2 is considered. For this case, the complex shows an oxidation potential very similar to the LNMO electrode. Therefore, the 1TMSPi:2LiDFOB case could provide the best balance between enhancing the sacrificial effect of these additives in both cathode and anode, thus protecting the electrolyte from further decomposition. It is important to note, however, that only isolated molecules have been considered here, and neither the cell environment nor the influence of other reactants and products have been considered. This is reflected in the over-

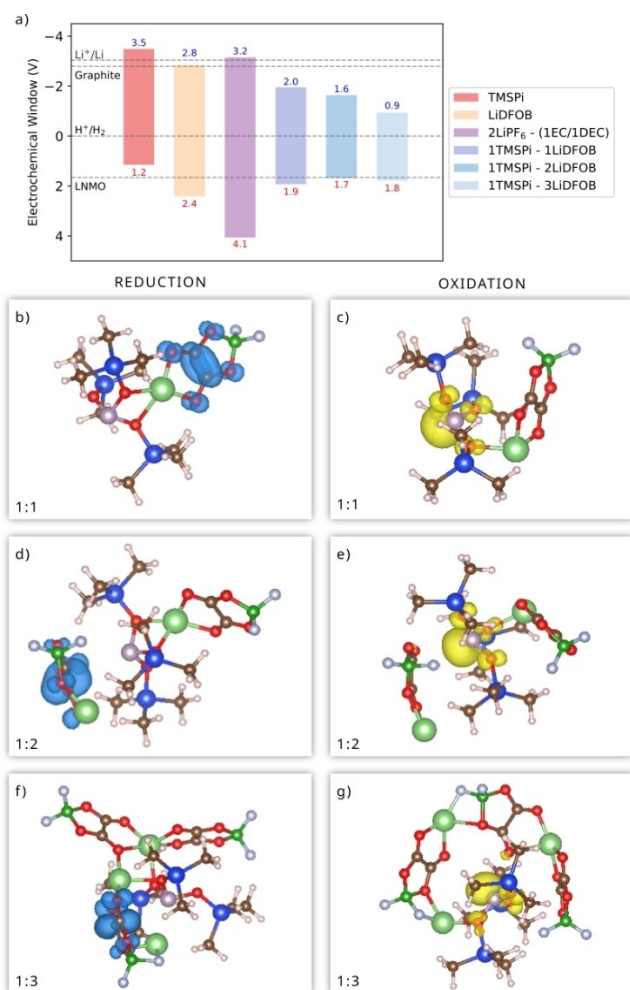


Figure 4. (a) Redox potentials for the TMSPi and LiDFOB additives, the electrolyte, and the TMSPi: LiDFOB complex with three different ratios of 1:1, 1:2, and 1:3. The dashed lines at -3.04 , -2.8 , 0.0 and 1.66 V represent, respectively, the reduction potential of the Li^+/Li , H^+/H , graphite and the LNMO electrode. Spin densities (isosurface = 0.005) for the reduced/oxidized states of the TMSPi: LiDFOB complex for the ratios 1:1 (b)/(c), 1:2 (d)/(e) and 1:3 (f)/(g). The following color scheme applies to the atoms: light green for lithium, green for bromine, light blue for fluorine, blue for silicon, light purple for phosphorus, red for oxygen, brown for carbon, and light pink for hydrogen.

estimated stability of $2\text{LiPF}_6\text{-(1EC/1DEC)}$. While accurately predicting the oxidation/reduction potentials is beyond the scope of this study, we can nevertheless study trends from these calculations.

Figure 4b–g shows the spin density plot for the three different ratios of the TMSPi: LiDFOB complex in the reduced (b, d, f) and oxidized (c, e, g) states. The ratios are shown in the respective cases. The spin density serves as an indication of where the charges would localize in each charge state, i.e., where the electron would be de/inserted during oxidation/reduction. As Figure 4b, d and f shows, the LiDFOB would be the reduced species, regardless of the ratio. Similarly, Figure 4c, e, and g present the TMSPi as the oxidized species for all different ratios.

Figure 5 shows dQ/dV plots obtained during the first part of the charge process of the formation cycle at 0.1 C to investigate the decomposition voltages of the electrolyte additives. The dQ/dV of different concentrations of additives and the baseline electrolyte are depicted in Figure S2. The dQ/dV plot is partitioned into two voltage ranges for more clear observations, i.e. Figure 5a in the range of $1\text{--}3.5$ V, whereas Figure 5b was in the range of $3.5\text{--}4.8$ V. A noteworthy fact is that during the formation cycle, in which the anode potential decreases dramatically during lithium intercalation while the cathode maintains at a relatively low potential, the electrolyte goes through a reduction reaction at the anode before being oxidized at the cathode at a higher potential. As a result of the reduction at a lower potential, an SEI is formed on the anode, which will further affect the performance of the cell.^[37] Thus, a study of an electrolyte additive should consider both its oxidation ability and its reduction reactions and how they may affect the subsequent oxidation and reduction processes of the electrolyte.^[37]

The additives resulted in voltage variations from the baseline electrolyte. dQ/dV intensities are observed for the baseline electrolyte starting at about 2.6 V; the prominent peak, having an apex at about 3 V, results from EC reduction at the graphite electrode. There is a noticeable peak when LiDFOB is being used (2.1 V vs. Li/Li^+), falling within the SEI formation range and at a higher voltage than the baseline electrolyte. Moreover, an oxidation peak at 4.4 V is observed during the first charging process, which likely represents the decomposition of TMSPi. A further change in the shape and position of the EC peak could be attributed to additive interactions with baseline components (EC, DEC, LiPF₆). Martin et al.^[17] showed that TMSPi interacts with the baseline electrolyte and forms species with different reduction potentials. Additionally, calculations of redox potentials have suggested that TMSPi would not be reduced at the anode,^[23] as is also seen in Figure 4a. Furthermore, it can be observed from Figure S2 that each concentration of additives resulted in different intense peaks at about 2.1 V and 4.4 V, which is in line with what has been observed in the DFT calculation (see Figure 4a). Besides that, CV results presented in Figure S2 confirmed the conclusion from dQ/dV results. Furthermore, in Figure 5c, the first galvanostatic charge/discharge profile of a cell with and without additives is compared. Noticeable plateaus at around 2.1 V and 4.65 V, corresponding to the decomposition of LiDFOB and TMSPi, respectively, during the first galvanostatic charge profile of a cell containing additives are observed.

Figure 6 displays the effect of the best-performing additive concentrations on the long-term cycling of an LNMO-graphite full-cells up to 400 cycles at room temperature. The discharge capacity retention improved with the addition of TMSPi and LiDFOB using a ratio of 1:2, reaching 100% after 120 cycles and 80% after 400 cycles. This is in contrast to the baseline electrolyte, which retained only 67% after 400 cycles. Furthermore, the cell with 1% TMSPi + 2% LiDFOB additives showed a higher average CE with $>99.7\%$ for over 400 cycles, in contrast to the cell without additives with a lower average CE of 99.4%. Note that the discharge capacities and CE of the first three

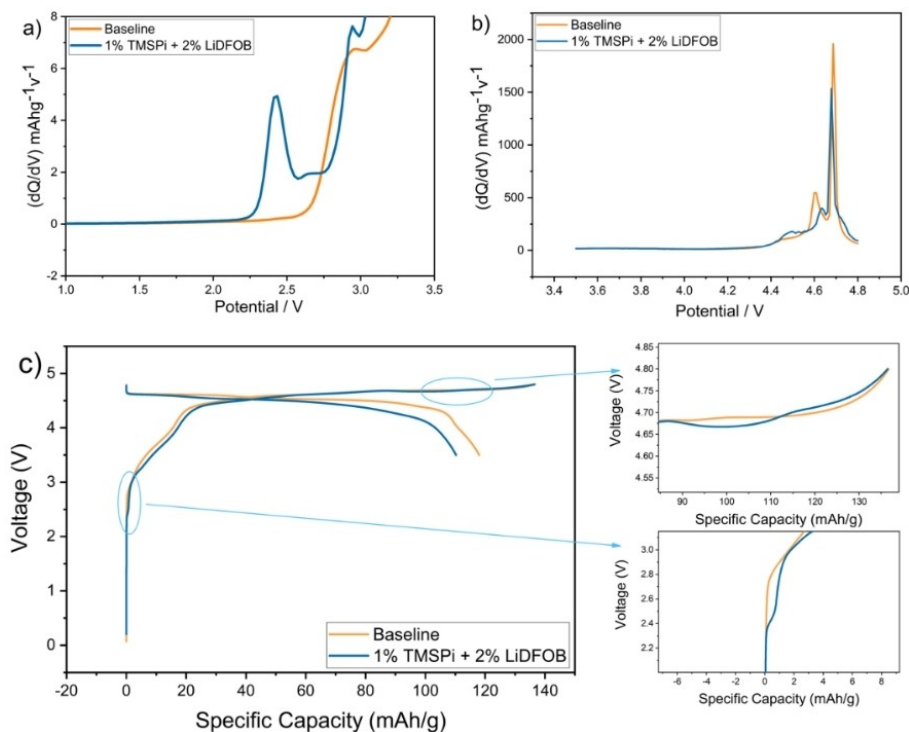


Figure 5. (a, b) dQ/dV curves of LNMO-graphite cells with and without additives during the first charge process to 4.8 V, (c) Initial charge/discharge curves of LNMO-graphite cells with and without additives.

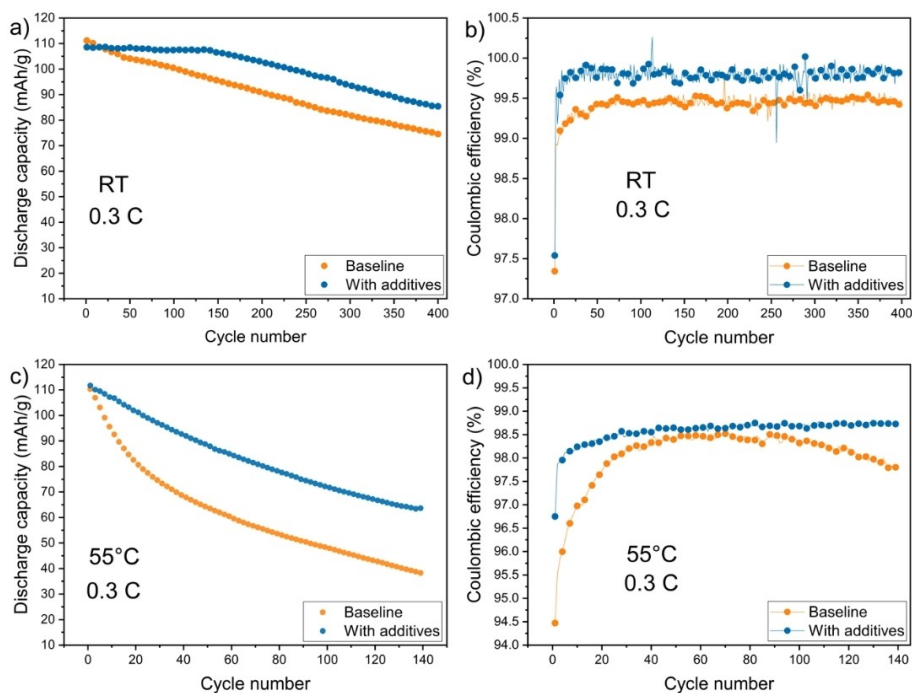


Figure 6. Discharge capacities and CE during galvanostatic cycling of LNMO-graphite cells with and without additives. The cells were cycled at (a, b) RT, and (c, d) at 55 °C.

formation cycles are provided in Table S1. It is observed that in Figure 6a, after ~150 cycle, the observed rate in capacity fade is slightly higher than the previous cycles. Previous studies suggest that this capacity fade could originate from a cyclable

lithium loss, which is limited in a full-cell.^[38] LiDFOB has been claimed as an electrolyte additive that improves the thermal stability of LIBs at elevated temperatures.^[25,39] This inspired us to investigate the cycle life of the LNMO-graphite full cells at a

high temperature of 55 °C as LNMO cells has shown to suffer from poor performance at high temperatures.^[38] As depicted in Figure 6c and d, the cell with the additives (1% TMSPI + 2% LiDFOB) shows a capacity retention of 60% after 140 cycles, in contrast to the cell with the baseline electrolyte, which exhibits only 30% capacity retention over the same cyclic period. This suggests that the additives mitigate the side reactions, e.g., the dissolution of the transition metal ions, at elevated temperatures and thus improve the cycling stability of the cell. It should be noted that the initial stable period is prolonged for cycling at RT, whereas it is virtually absent at 55 °C. According to earlier research, the initial stable cycling that results from the anode's excess capacity allows for the electrode imbalance caused by LNMO self-discharge during cycling, but only for a certain amount of time. In contrast, it occurs only during the formation cycles at 55 °C.^[38,40]

Galvanostatic charge-discharge cycling was combined with ICI to investigate the internal resistances of the cell with and without additive (1% TMSPI + 2% LiDFOB). A plot of cell resistance versus cell capacity after three formation cycles can be seen in Figure 7. The ICI measurements were carried out at a rate of 0.3 C. The ICI measurements for the three formation cycles (0.1 C) of both cells are shown in Figure S4. The results show that the cell with additives has a slightly higher internal resistance than the baseline cell. Consequently, the results reinforce our conclusion that the products of the additives/electrolyte interaction contribute to CEI/SEI formation. It can be seen from the result that the cell containing additives has approximately the same high resistance at the beginning of the discharge (on cycles 1, 50, and 100), and then stabilize as the discharge continues. The increase in resistance can be attributed to the deposition of insoluble products produced by the decomposition of the electrolyte components together with the additives. However, both electrode resistances show a minor increase from the 50th to 100th cycles.

To gain further insight into the differences between the surface chemistries of the LNMO-graphite electrodes with and without the additives, scanning electron microscopy (SEM) and XPS were carried out on the cycled electrodes. The SEM images of the cycled electrode, shown in Figure S5, demonstrate that the morphology of active particles and conductive carbon does not differ on the LNMO and graphite surfaces before and after

cycling, implying that the additives do not have a significant impact on the global electrode structure. However, the XPS results show that they influence the chemistry of the surface layers.

The XPS survey spectra presented in Figure S6a shows that intensity Na 1s peak originated from CMC binder decreased from pristine to cycled samples for both LNMO and graphite electrodes indicating formation of CEI and SEI, respectively. On LNMO, CEI is thicker when the TMSPI (1 wt.%) and LiDFOB (2 wt.%) additives are included in the electrolyte, because the intensity of Na 1s peak is decreased compared to the spectra of LP40 sample, and Mn 2p spectra is diminished.^[41] This could be the reason behind the high internal resistance as observed in the ICI experiment, and could also advocate less dissolution of Mn into the electrolyte (Figure S6b, top image no cross talk of Mn over graphite surface). On graphite, no Na 1s peak is detected for the cycled graphite in the baseline electrolyte indicating SEI is thicker than probing depth of the XPS analysis (i.e., about 10 nm). The presence of Mn 2p peak at 650 eV on graphite cycled in the baseline electrolyte confirms dissolution of manganese from LNMO into the electrolyte which is later deposited on graphite. Such peak is absent on the graphite cycled in the electrolyte with the additives. Also, based upon the ratio between the C 1s and F 1s peaks, it can be inferred that the SEI for the baseline electrolyte is C-enriched, while it is F-enriched for the additive containing electrolyte.

Figure 8a and b represent the C 1s, F 1s, O 1s, P 2p and Li 1s spectra for the LNMO and graphite electrodes, respectively. The C 1s, P 2p and Li 1s spectra of cycled LNMO electrode showed similar features in the baseline LP40 electrolyte and additive containing electrolyte, while the main differences can be seen in the F 1s, O 1s and Li 1s spectra. The F 1s spectra show the presence of LiF on the surface of LNMO in the baseline electrolyte, while the corresponding peak at 685 eV was not detected from LNMO cycled in the electrolyte with additives. The O 1s spectra show that the ratio between C=O to C–O containing species decreases from the baseline to the electrolyte with the additives. The main peak in the Li 1s spectra is slightly shifted to higher binding energies for LNMO for the electrolyte with the additive as compared to that from the baseline electrolyte, indicating CEI is more LiF enriched. The XPS spectra of the graphite electrodes on the other hand show

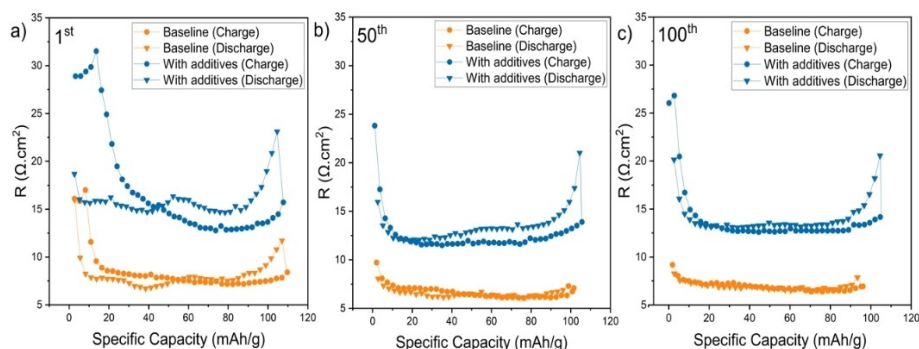


Figure 7. Resistance profiles of LNMO-graphite full-cells at different cycles with and without additives at 0.3 C after three formation cycles at 0.1 C.

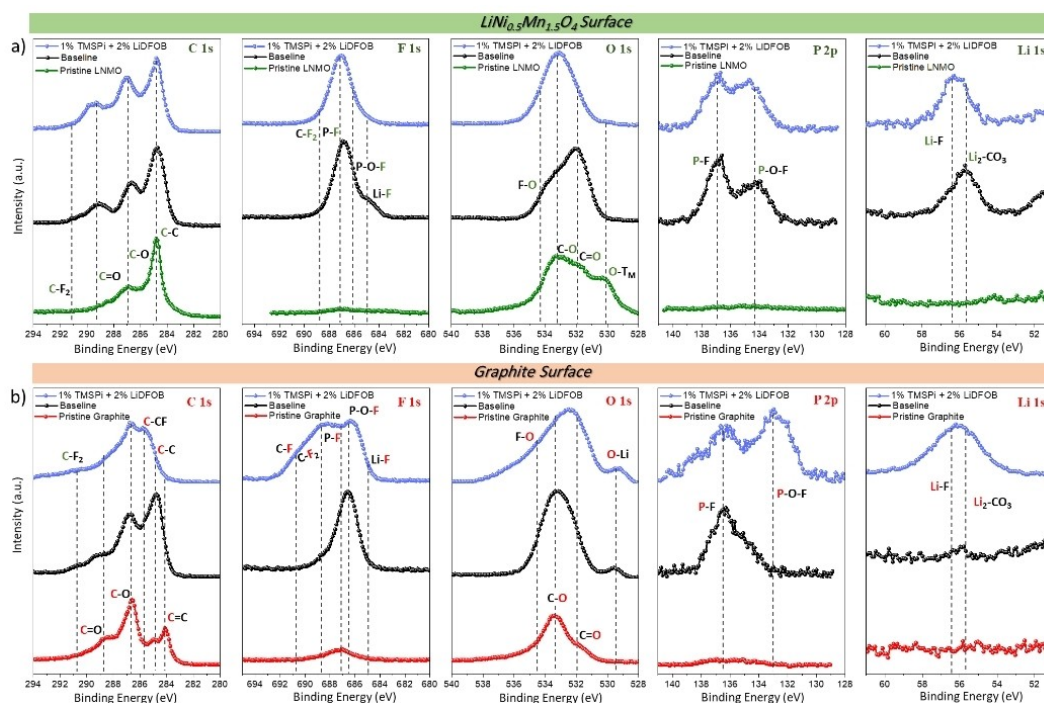


Figure 8. (a) C 1s, F 1s, O 1s, P 2p and Li 1s XPS spectra of the pristine and cycled LNMO cathode in the electrolytes with and without additives. (b) C 1s, F 1s, O 1s, P 2p and Li 1s spectra of the pristine and cycled graphite anode in the electrolytes with or without additives.

more significant differences for the graphite electrodes cycled in electrolyte with and without the additives. The C 1s, O 1s, F 1s, and P 2p spectra show formation of a larger variety of species on graphite electrode cycled in the electrolyte with the additive. The additive containing electrolyte enabled formation of $\text{Li}_x\text{PF}_y\text{O}_z$ (P–O–F in Figure 8b, O 1s, F 1s and P 2p) which could not be detected on the surface of graphite electrode cycled in the baseline electrolyte. This observation agrees with previous literatures suggesting that TMSPI reacts with the $[\text{PF}_6]^-$ anions and forms LiPF_xO_y .^[35,42] The LiDFOB (2 wt.%) in the carbonate-based electrolyte is known to form F–B based species which strengthens these surface film and prevents further decomposition of electrolyte as well as suppresses dissolution of Mn (see Figure S6b, the top images display no Mn at the graphite surface).^[27,29,43] The other difference in the composition of SEI is the presence of the peak at 688.8 eV in the F 1s spectra for the additive containing electrolyte, which is likely originated from fluorine-containing organic species (C–F₂) formed by decomposition of additives.^[35,44]

Overall, the function of electrolyte additives is to provide extra by-products of decomposition that aid in the yield of dense, thin, and ionically conducting interphase layers on both electrode surfaces. The complexity of decomposition products formation and the subsequent restructuring of these films during cycling make it challenging to pinpoint the precise role of the additive. On the other hand, when utilized in high-voltage materials, a tunable interphase layer might not be created by a single additive alone on both electrodes. Therefore, using dual additives could provide different functions through the synergistic effect of additives. Nonetheless, the

performance of the SEI/CEI film is not only determined by the amount of additives but also by the complexation ratio and interaction between two or more additives, which needs further investigation. However, since the OP and RP values of the additive combination differ from those of each individual additive (as illustrated in Figure 4a), it is probable that the interaction effect observed when using TMSPI and LiDFOB in conjunctions will not be observed when TMSPI or LiDFOB is used individually (as shown in Figure S7). Though the decomposition mechanism of TMSPI or LiDFOB via redox reaction have previously been discussed in literatures,^[17,27,35,45] understanding the details of decomposition reactions in the presence of combined additive remains as a challenge. We, therefore, think that the qualities and selection standards made in this study can be applied to the selection of additive materials with a similar mechanism for enhancing the performance of the cell in high-voltage LIBs.

One of the main limitations of this study was the degradation observed in the LP40 electrolyte containing TMSPI over time during storage. Similar to other studies,^[17] a detrimental reaction between TMSPI and LiPF_6 was observed, but further characterization of this reaction was beyond the scope of this study. This reaction limits the use of TMSPI as an additive to only freshly prepared electrolytes.

Conclusions

TMSPI and LiDFOB were used as electrolyte additives to improve the electrochemical performance of the $\text{LiNi}_{0.5}\text{Mn}_{1.5}\text{O}_4$ -

graphite full-cells in the voltage range of 3.5–4.8 V. The best-performance concentration of 1 wt.% TMSPI and 2 wt.% LiDFOB improved the capacity retention at long-term cycling at room temperature and at 55 °C. The XPS spectra, resistance measurement results combined with computational findings indicate decomposition of the electrolyte additive to contribute to the formation of surface layers on LNMO and graphite electrodes. NMR spectra of the electrolytes suggest that the presence of different complexes derives from the interaction of electrolyte components with different concentrations of additives. According to NMR results, the performance of the SEI/CEI film is largely determined not only by the amount of additives but also by the complexation ratio and interaction between the two additives. Thus, the complexes, namely, TMSF, TMSPa, BMSPa, and MMSPa, derived from 1 wt.% TMSPI and 2 wt.% LiDFOB appear to be the most favorable for providing proper SEI/CEI films. Furthermore, DFT calculations exhibit that the concentration of 1 wt.% TMSPI and 2 wt.% LiDFOB provides the best reduction/oxidation potential values when compared to other concentrations, thus significantly affecting the electrochemical performance of the cell. We anticipate that this study may offer a practical and reproducible research approach for new applications of high-energy-density LIBs.

Experimental Section

Electrode and electrolyte preparation and electrochemical cells

LNMO powder was obtained from Haldor Topsøe A/S, Denmark. Carboxymethyl cellulose (CMC) was sourced from Leclanché. The LNMO electrodes were prepared by mixing a slurry containing 90 wt.% LNMO, 5 wt.% of super C65 (CABOT), and 5 wt.% CMC in de-ionized water using a MM mixer mill (Retsch) at 25 Hz for 30 min. A doctor blade was used to cast the slurry on carbon-coated Al foil (20 μm thick). The coating was then dried overnight at 75 °C to evaporate any remaining solvent. 20 mm diameter electrodes were punched from the coating, calendared at a pressure of 1.59 toncm⁻², and then dried in a Büchi oven at 120 °C for 12 h under vacuum. The active mass loading was around ~10.5 mg cm⁻² (1.5 mAh cm⁻²). Graphite powder was obtained from Imerys (GDHR 15–4 graphite). The graphite electrodes were obtained by coating the aqueous slurry of graphite powder, C65 carbon black, and CMC binder in the weight ratio of 92:3:5, respectively, on a C-coated Cu foil. The coatings were then dried at 75 °C overnight. Graphite electrodes of 22 mm were punched out and then dried in a Büchi oven in an Ar-filled glovebox at 120 °C for at least 12 h under vacuum. The capacity loading of graphite electrodes was approximately 1.8–2 mAh cm⁻².

1 M LiPF₆ in EC/DEC 1:1 by weight, Solvionic, purity: 99.9% was used as the baseline electrolyte. 1 wt.% of tris(trimethylsilyl) phosphite (TMSPI, Sigma-Aldrich; purity: 95%) and different amounts (1 to 3 wt.%) of lithium difluoro (oxalato) borate (LiDFOB, Sigma-Aldrich; purity: 95%) were added to the baseline electrolyte. Over a period of ~12 hours, the electrolyte was stirred in Al vials (dried overnight). It should be noted that additives-containing electrolyte needs to be used fresh, as it has been stated by Martin et al. that TMSPI has a limited lifespan when used in a conventional LiPF₆-containing carbonate-based electrolyte.^[17] The electrolyte preparation and the pouch cell assembly were carried out in an Ar-

filled glovebox (H₂O and O₂ < 1 ppm). For each cell, 120 μL of electrolyte solution was used. The separator was constructed using two layers of microporous polypropylene film with a 4 × 4 cm² area (Celgard 2500). The separators were dried for 6 hours in a Büchi oven at 70 °C before being used.

Electrochemical measurements

The LNMO-graphite pouch cells were galvanostatically cycled between 3.5 V to 4.8 V using a battery cyclor (BT-2000, Arbin, USA). The cells were cycled with three formation cycles at 0.1 C using the constant current (CC) mode. Subsequently, the cells were charged-discharged at 0.3 C via a constant current (~0.5 mA) and constant voltage (4.8 V) (CC–CV) mode. The constant voltage was applied at 4.8 V until the current decreased to a current equal to the 0.1 C rate for that cell. The ICI (intermittent current interruption) method was used to measure the internal resistance of the cell by applying a regular pause every 5 min for 1 s according to the procedure developed by M. J. Lacey.^[46] Measurement and galvanostatic charge-discharge cycling were performed at room temperature and 55 °C. Cyclic voltammograms (CV) test was carried out on pouch cell using C-coated Cu foil vs. lithium metal between 0–3 V with and without additives (TMSPI:LiDFOB, 1:2 by weight) and C-coated Al foil vs. lithium metal – between 3–5 V with and without additives, at a scan rate of 0.05 mV/s.

NMR spectroscopy

NMR spectra were collected using a Jeol Delta 400 MHz NMR spectrometer at 298 K. The chemical shifts were specified in parts per million (ppm) and coupling constants (J values) in hertz (Hz). All samples were prepared using pre-dried solvents and additives in an argon-filled glovebox. All NMR tubes were dried in a vacuum at 60 °C. The electrolyte (400 μL) was transferred into the NMR tube (5 mm thin wall 7" 1000 MHz, Wildmad). The 100 μL NMR solvent (deuterium oxide, D₂O) was filled into a coaxial NMR insert (Wildmad) and then inserted into the NMR tube. Both the NMR tube and the NMR insert were tightly sealed with their caps and Parafilm tape for measurements with the NMR spectrometer. The ¹H NMR spectra were acquired with a recycling delay of 5 s, frequency of 399.78 MHz, and 64 number of scans. The ¹³C NMR spectra were acquired with a recycling delay of 2 s, frequency of 100.53 MHz, and 64 number of scans. The ¹⁹F NMR spectra were acquired with a recycling delay of 5 s, frequency of 376.17 MHz, and 16 number of scans. The ³¹P NMR spectra were acquired with a recycling delay of 5 s, frequency of 161.83 MHz, and 16 number of scans.

Computational details

The redox potentials were calculated within the density functional theory scope following the reduction reaction Gibbs free energy associated with the corresponding redox pairs. Nernst equation [Eq. (1)]:

$$E^0 = -\frac{\Delta G_{(\text{soln})}(\text{Red})}{nF} \quad (1)$$

was employed according to the N/Red (Ox/N) convention to evaluate the reduction (oxidation) process, in which N, Red, and Ox are, respectively, the neutral, reduced, and oxidized states of the investigated complex. In Equation (1), *F* and *n* stands for the Faraday's constant and the number of electrons involved in the reaction, respectively. The reduction free energy in solution was

considered following the Born-Haber thermodynamic cycle, similar to previous works.^[47] The Gibbs free energy of the different systems/states is described by Equation (2):

$$G = E_{\text{elect}} + E_{\text{ZPE}} + PV + U_{298} - TS_{298} \quad (2)$$

in which the first, second, and third terms on the right-hand side are the electronic total energy, zero-point energy, and the pressure-volume product. The contributions for the internal energy U and entropy TS terms have been considered for the finite 298 K temperature, including translational, rotational, and vibrational degrees of freedom. These quantities have been obtained through density functional theory (DFT) calculations according to the following steps: (i) first, a full geometry optimization was carried out for all the charge states considering the wB97XD^[48] long-range corrected hybrid exchange-correlation functional and the 6-31G(d) basis set;^[49,50] (ii) in sequence, the thermal corrections were evaluated from the vibrational frequencies following the same theory level; (iii) a single-point calculation was then performed at a higher theory level wB97XD/6-311G(d,p)^[51–53] to get a better description of the electronic energy; (iv) finally, the solvation energies were calculated using the SMD^[54] continuum solvation model having acetonitrile as solvent. These calculations were performed within the Gaussian 16 software package.^[55]

Scanning electron microscopy

The morphology of the surface film on LNMO and graphite electrodes was examined by a Zeiss 1550 Scanning Electron Microscope (SEM). The pristine and cycled (at RT) LNMO and graphite electrodes were harvested from the LNMO-graphite cells, which were opened in an Ar-filled glovebox and then rinsed with DMC three times, each time using 4–5 drops to remove electrolyte residues. The electrodes were placed on carbon tape after the DMC had dried off. In sealed glass vials, specimens were transferred to the SEM and exposed to air for 15–20 seconds before being moved to the SEM chamber. The SEM images were obtained at an accelerating voltage of 4 kV, and the analysis was conducted at a 4 mm working distance.

X-ray photoelectron spectroscopy

The initial chemical composition of the surface film on LNMO and the graphite electrode were measured by XPS. The cycled (100 cycles) LNMO-graphite electrodes were disassembled in an argon-filled glovebox, and retrieved electrodes were rinsed carefully with dimethyl carbonate (DMC) three times to remove remaining electrolyte. The samples were transferred to the XPS in a plane dual-height sample holder built to hold a vacuum during transfer to prevent air exposure. Pristine and cycled LNMO and graphite electrodes were analyzed using a Kratos AXIS Supra + X-ray photoelectron spectroscopy (XPS) instrument with monochromatized Al K α radiation (1486.6 eV) using 15 mA filament current. The obtained spectra for each element were internally calibrated considering the C 1s peak and a C–C binding energy at 284.8 eV.

Acknowledgments

The authors would like to acknowledge STandUP for Energy via the Swedish Energy Agency and CoFBAT, which is an EU-funded project that has received funding from the European Union's Horizon 2020 Research and Innovation Programme under Grant

Agreement N. 875126. The impartial financial support provided by Volkswagen AG and Scania CV AB are gratefully acknowledged.

Conflict of Interest

The authors declare no conflict of interest.

Data Availability Statement

The data that support the findings of this study are available from the corresponding author upon reasonable request.

Keywords: lithium-ion batteries · electrolyte additives · tris(trimethylsilyl) phosphite · lithium difluoro(oxalato)borate · graphite

- [1] F. Wu, J. Maier, Y. Yu, *Chem. Soc. Rev.* **2020**, *49*, 1569–1614.
- [2] A. Kuwabara, M. Enomoto, E. Hosono, K. Hamaguchi, T. Onuma, S. Kajiyama, T. Kato, *Chem. Sci.* **2020**, *11*, 10631–10637.
- [3] D. Carlier, A. Van der Ven, C. Delmas, G. Ceder, *Chem. Mater.* **2003**, *15*, 2651–2660.
- [4] C.-C. Su, M. He, P. C. Redfern, L. A. Curtiss, I. A. Shkrob, Z. Zhang, *Energy Environ. Sci.* **2017**, *10*, 900–904.
- [5] W. Sun, Y. Li, Y. Liu, Q. Guo, S. Luo, J. Yang, C. Zheng, K. Xie, *J. Mater. Chem. A* **2018**, *6*, 14155–14161.
- [6] J. Li, L. Baggetto, S. K. Martha, G. M. Veith, J. Nanda, C. Liang, N. J. Dudney, *Adv. Energy Mater.* **2013**, *3*, 1275–1278.
- [7] S. Deng, B. Xiao, B. Wang, X. Li, K. Kaliyappan, Y. Zhao, A. Lushington, R. Li, T.-K. Sham, H. Wang, X. Sun, *Nano Energy* **2017**, *38*, 19–27.
- [8] Y. Ma, K. Chen, J. Ma, G. Xu, S. Dong, B. Chen, J. Li, Z. Chen, X. Zhou, G. Cui, *Energy Environ. Sci.* **2019**, *12*, 273–280.
- [9] B. Xiao, H. Liu, J. Liu, Q. Sun, B. Wang, K. Kaliyappan, Y. Zhao, M. N. Banis, Y. Liu, R. Li, T.-K. Sham, G. A. Botton, M. Cai, X. Sun, *Adv. Mater.* **2017**, *29*, 1703764.
- [10] W. Liu, Q. Shi, Q. Qu, T. Gao, G. Zhu, J. Shao, H. Zheng, *J. Mater. Chem. A* **2017**, *5*, 145–154.
- [11] J. Mou, Y. Deng, Z. Song, Q. Zheng, K. H. Lam, D. Lin, *Dalton Trans.* **2018**, *47*, 7020–7028.
- [12] K. Edström, T. Gustafsson, J. O. Thomas, *Electrochim. Acta* **2004**, *50*, 397–403.
- [13] D. R. Gallus, R. Wagner, S. Wiemers-Meyer, M. Winter, I. Cekic-Laskovic, *Electrochim. Acta* **2015**, *184*, 410–416.
- [14] X. Zuo, C. Fan, J. Liu, X. Xiao, J. Wu, J. Nan, *J. Electrochem. Soc.* **2013**, *160*, A1199–A1204.
- [15] Z. Cai, Y. Liu, J. Zhao, L. Li, Y. Zhang, J. Zhang, *J. Power Sources* **2012**, *202*, 341–346.
- [16] D. J. Lee, D. Im, Y.-G. Ryu, S. Lee, J. Yoon, J. Lee, W. Choi, I. Jung, S. Lee, S.-G. Doo, *J. Power Sources* **2013**, *243*, 831–835.
- [17] X. Qi, L. Tao, H. Hahn, C. Schultze, D. R. Gallus, X. Cao, S. Nowak, S. Röser, J. Li, I. Cekic-Laskovic, B. R. Rad, M. Winter, *RSC Adv.* **2016**, *6*, 38342–38349.
- [18] S. Mai, M. Xu, X. Liao, J. Hu, H. Lin, L. Xing, Y. Liao, X. Li, W. Li, *Electrochim. Acta* **2014**, *147*, 565–571.
- [19] J. Welch, R. Mogensen, W. van Ekeren, H. Eriksson, A. J. Naylor, R. Younesi, *J. Electrochem. Soc.* **2022**, *169*, 120523.
- [20] Y. M. Song, J. G. Han, S. Park, K. T. Lee, N. S. Choi, *J. Mater. Chem. A* **2014**, *2*, 9506–9513.
- [21] Y. Okamoto, Y. Kubo, *ACS Omega* **2018**, *3*, 7868–7874.
- [22] K. Ozawa, *Lithium Ion Rechargeable Batteries: Materials, Technology, New Applications*, Wiley, **2010**.
- [23] Y.-K. Han, J. Yoo, T. Yim, *J. Mater. Chem. A* **2015**, *3*, 10900–10909.
- [24] B. Koo, J. Lee, Y. Lee, J. K. Kim, N.-S. Choi, *Electrochim. Acta* **2015**, *173*, 750–756.
- [25] Z. Chen, Y. Qin, J. Liu, K. Amine, *Electrochem. Solid-State Lett.* **2009**, *12*, A69.

- [26] L. Bodenes, R. Dedryvère, H. Martinez, F. Fischer, C. Tessier, J.-P. Pérès, *J. Electrochem. Soc.* **2012**, *159*, A1739–A1746.
- [27] S. S. Zhang, *J. Power Sources* **2007**, *163*, 713–718.
- [28] D. P. Abraham, M. M. Furczon, S. H. Kang, D. W. Dees, A. N. Jansen, *J. Power Sources* **2008**, *180*, 612–620.
- [29] M. H. Fu, K. L. Huang, S. Q. Liu, J. S. Liu, Y. K. Li, *J. Power Sources* **2010**, *195*, 862–866.
- [30] D. Y. Wang, J. R. Dahn, *J. Electrochem. Soc.* **2014**, *161*, A1890–A1897.
- [31] D. Y. Wang, N. N. Sinha, R. Petibon, J. C. Burns, J. R. Dahn, *J. Power Sources* **2014**, *251*, 311–318.
- [32] W. Wahyudi, X. Guo, V. Ladelata, L. Tsetseris, M. I. Nugraha, Y. Lin, V. Tung, N. Hadjichristidis, Q. Li, K. Xu, J. Ming, T. D. Anthopoulos, *Adv. Sci.* **2022**, *9*, 2202405.
- [33] N. Gogoi, E. Bowall, R. Lundström, N. Mozhzhukhina, G. Hernández, P. Broqvist, E. J. Berg, *Chem. Mater.* **2022**, *34*, 3831–3838.
- [34] H. Cheng, Q. Sun, L. Li, Y. Zou, Y. Wang, T. Cai, F. Zhao, G. Liu, Z. Ma, W. Wahyudi, Q. Li, J. Ming, *ACS Energy Lett.* **2022**, *7*, 490–513.
- [35] A. Guéguen, C. Bolli, M. A. Mendez, E. J. Berg, *ACS Appl. Energ. Mater.* **2020**, *3*, 290–299.
- [36] S. Tan, Z. Shadike, J. Li, X. Wang, Y. Yang, R. Lin, A. Cresce, J. Hu, A. Hunt, I. Waluyo, L. Ma, F. Monaco, P. Cloetens, J. Xiao, Y. Liu, X. Q. Yang, K. Xu, E. Hu, *Nat. Energy* **2022**, *7*, 484–494.
- [37] S. A. Delp, O. Borodin, M. Olguin, C. G. Eisner, J. L. Allen, T. R. Jow, *Electrochim. Acta* **2016**, *209*, 498–510.
- [38] B. Aktekin, M. J. Lacey, T. Nordh, R. Younesi, C. Tengstedt, W. Zipprich, D. Brandell, K. Edström, *J. Phys. Chem. C* **2018**, *122*, 11234–11248.
- [39] S. Shui Zhang, *Electrochem. Commun.* **2006**, *8*, 1423–1428.
- [40] J. H. Kim, N. P. W. Pieczonka, Z. Li, Y. Wu, S. Harris, B. R. Powell, *Electrochim. Acta* **2013**, *90*, 556–562.
- [41] G. D. Salian, J. Højberg, C. Fink Elkjær, Y. Tesfamhret, G. Hernández, M. J. Lacey, R. Younesi, *ChemistryOpen* **2022**, *11*, 1–8.
- [42] T. J. Lee, J. Soon, S. Chae, J. H. Ryu, S. M. Oh, *ACS Appl. Mater. Interfaces* **2019**, *11*, 11306–11316.
- [43] M. Hu, J. Wei, L. Xing, Z. Zhou, *J. Appl. Electrochem.* **2012**, *42*, 291–296.
- [44] G. Beamson, D. Briggs, *High Resolution XPS of Organic Polymers: The Scienta ESCA300 Database*, Wiley, **1992**.
- [45] C. Peebles, R. Sahore, J. A. Gilbert, J. C. Garcia, A. Tornheim, J. Bareño, H. Iddir, C. Liao, D. P. Abraham, *J. Electrochem. Soc.* **2017**, *164*, A1579–A1586.
- [46] M. J. Lacey, *ChemElectroChem* **2017**, *4*, 1997–2004.
- [47] C. F. N. Marchiori, R. P. Carvalho, M. Ebadi, D. Brandell, C. M. Araujo, *Chem. Mater.* **2020**, *32*, 7237–7246.
- [48] J.-D. Chai, M. Head-Gordon, *J. Chem. Phys.* **2008**, *128*, 084106.
- [49] M. M. Francl, W. J. Pietro, W. J. Hehre, J. S. Binkley, M. S. Gordon, D. J. DeFrees, J. A. Pople, *J. Chem. Phys.* **1982**, *77*, 3654–3665.
- [50] W. J. Hehre, K. Ditchfield, J. A. Pople, *J. Chem. Phys.* **1972**, *56*, 2257–2261.
- [51] M. J. Frisch, J. A. Pople, J. S. Binkley, *J. Chem. Phys.* **1984**, *80*, 3265–3269.
- [52] R. Krishnan, J. S. Binkley, R. Seeger, J. A. Pople, *J. Chem. Phys.* **1980**, *72*, 650–654.
- [53] A. D. McLean, G. S. Chandler, *J. Chem. Phys.* **1980**, *72*, 5639–5648.
- [54] A. V. Marenich, C. J. Cramer, D. G. Truhlar, *J. Phys. Chem. B* **2009**, *113*, 6378–6396.
- [55] M. J. Frisch, G. W. Trucks, H. B. Schlegel, G. E. Scuseria, M. A. Robb, J. R. Cheeseman, G. Scalmani, V. Barone, G. A. Petersson, H. Nakatsuji, *Inc., Wallingford CT* **2016**, 2016.

Manuscript received: March 29, 2023

Revised manuscript received: June 2, 2023

Version of record online: June 27, 2023